

Accepted Manuscript

Title: Ru Subnanoparticles on N-doped Carbon Layer Coated SBA-15 as Efficient Catalysts for Arene Hydrogenation

Authors: Wei Qian, Lina Lin, Yunxiang Qiao, Xiuge Zhao, Zichen Xu, Honghui Gong, Difan Li, Manyu Chen, Rong Huang, Zhenshan Hou



PII: S0926-860X(19)30338-2
DOI: <https://doi.org/10.1016/j.apcata.2019.117183>
Article Number: 117183

Reference: APCATA 117183

To appear in: *Applied Catalysis A: General*

Received date: 10 May 2019
Revised date: 5 July 2019
Accepted date: 27 July 2019

Please cite this article as: Qian W, Lin L, Qiao Y, Zhao X, Xu Z, Gong H, Li D, Chen M, Huang R, Hou Z, Ru Subnanoparticles on N-doped Carbon Layer Coated SBA-15 as Efficient Catalysts for Arene Hydrogenation, *Applied Catalysis A, General* (2019), <https://doi.org/10.1016/j.apcata.2019.117183>

This is a PDF file of an unedited manuscript that has been accepted for publication. As a service to our customers we are providing this early version of the manuscript. The manuscript will undergo copyediting, typesetting, and review of the resulting proof before it is published in its final form. Please note that during the production process errors may be discovered which could affect the content, and all legal disclaimers that apply to the journal pertain.

Ru Subnanoparticles on N-doped Carbon Layer Coated SBA-15 as Efficient Catalysts for Arene Hydrogenation

Wei Qian,^a Lina Lin,^b Yunxiang Qiao,^c Xiuge Zhao,^a Zichen Xu,^a Honghui Gong,^a Difan Li,^a Manyu Chen,^a Rong Huang,^{b*} Zhenshan Hou^{a,*}

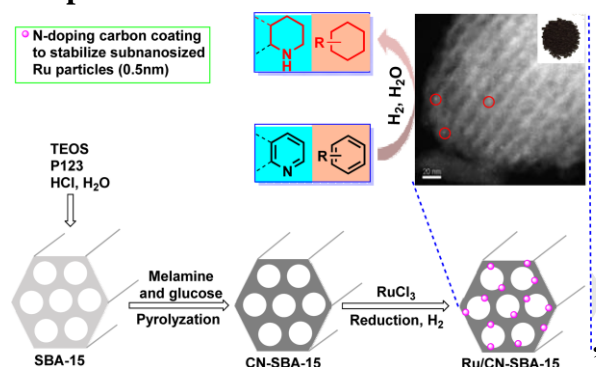
^aKey Laboratory for Advanced Materials, Research Institute of Industrial Catalysis, School of Chemistry and Molecular Engineering, East China University of Science and Technology, Shanghai 200237, China. E-mail:houzhenshan@ecust.edu.cn.

^bKey Laboratory of Polar Materials and Devices, Ministry of Education, East China Normal University, Shanghai 200062, China.

^cMax-Planck-Institut für Kohlenforschung, Kaiser-Wilhelm-Platz 1, 45470 Mülheim an der Ruhr, Germany

* Corresponding author. E-mail address: houzhenshan@ecust.edu.cn (Z. Hou).

Graphical abstract



Highlights

- ◆ The N-doped carbon layer coated SBA-15 support has been developed;
- ◆ The Ru was loaded on the support with an ultra-low loading (*ca.* 0.1 wt.%);
- ◆ The uniform sub-1-nm Ru particles (0.5 nm) are achieved on the support;
- ◆ The Ru catalyst showed an exceptionally high TOF and good recyclability;
- ◆ The activity enhanced dramatically with decreasing the sizes of Ru particles.

Abstract

The N-doped carbon layer coated SBA-15 support has been accomplished via a pyrolysis process. The ultra-low loading Ru nanoparticles (*ca.* 0.1 wt.%) was

incorporated into the support by impregnation and the sequential reduction. The images of HAADF-STEM revealed that the Ru particles with sub-1-nm size (0.2-0.7 nm) were uniformly dispersed on the support. The ultrafine Ru particles displayed the excellent activity for the hydrogenation of olefins, arenes, phenol derivatives and heteroarenes in aqueous phase. The aliphatic or alicyclic compounds were produced selectively without the hydrogenolysis of C–O and C–N bonds. The high turnover frequency (TOF) values can reach up to 10000 h⁻¹. Notably, the activity of these catalysts improved dramatically with decreasing the sizes of Ru particles. Meanwhile, the N-doped carbon layer coating endowed the high stability of the Ru catalysts and prevented the leaching of the Ru species owing to the strong interaction between doped-N atoms and the ultrafine Ru particles. Overall, this work provides a highly attractive strategy to construct the supported sub-1-nm Ru particles utilized for the aqueous hydrogenation.

Keywords: Arenes; N-Heteroarenes; Hydrogenation; Ru Subnanoparticles; N-doped carbon layers; SBA-15.

1. Introduction

Hydrogenation of arenes and heteroarenes is an indispensable method of organic synthesis on both laboratory and industrial scales, including plastics, explosives and natural product synthesis [1-3], which executes the rapid production of substituted cyclohexane derivatives and converts sustainable raw biomass into valuable resources. Hence, development of effective approach to the high conversion of arenes and heteroarenes to high-value chemicals has aroused considerable public concern [4]. In general, these unsaturated hydrogenation reactions are operated by using heterogeneous catalysts that include transition-metal particles dispersed on solid supports with a large surface area [5]. It is well known that noble metals are as efficient hydrogenation catalysts, which can easily convert various unsaturated organic compounds. However, noble metal catalysts are extremely expensive and have uneven distribution [6], and

thus it is particularly required to replace these noble metals with less noble alternatives or an ultra-low loading of noble metal. Moreover, in addition to reducing the use of noble metal content, the selection of catalyst support is also imperative, which can facilitate the utilization efficiency of metal atoms and enhance the activity of catalysts by synthesizing truly uniform sub-nanosized metal nanoparticles [7]. Unfortunately, the research on these aspects remains poorly understood.

It has been demonstrated that the catalytic performance of the metal nanoparticles are highly dependent on the size distributions and metal-support interactions [8]. Normally, a decrease in size of metal nanoparticles provides an effective approach to achieve a high surface-to-volume ratio [9], and thus leading to higher efficiency for catalytic reaction. Great effort has been contributed to achieving noble metal nanoparticles with sizes smaller than 2 nm, which typically involves the use of organic capping molecules or polymeric stabilizers [10]. Ru nanoparticles play an important role in many catalytic reactions, especially in hydrogenation of C=C, C=O and C=N double bonds in olefins/arenes, carbonyls and N-heterocycle compounds [11]. Although Ru nanoparticles of variable size have been synthesized using stabilizing agents including ionic liquids (ILs) and some organic ligands [10,12] the immobilization of catalytically active Ru particles with the size in the sub-1-nm regime on solid supports is a huge challenge [13].

In the supported metal catalysts, in addition to owing good catalytic behavior, how to stabilize the metal species and prevent aggregation through the supports is also a very important factor [14,15]. Moreover, the inorganic supports like alumina, silica, and zeolites could typically not be stable in the aqueous solution under the elevated temperature and pressure conditions [16,17]. Recently, carbon-supported metal nanoparticles as effective hydrogenation catalysts have also earned considerable interest [18]. Nevertheless, the weak interactions between the metal and carbon could result in leaching and/or agglomerating of metals [19,20]. To stabilize the metal nanoparticles, surface modification of the carbon materials was suggested by incorporation of heteroatoms, especially for nitrogen owing to its one lone electron pair that may coordinate with the unoccupied d orbital of metal [21,22]. But metal loaded

on carbon or nitrogen-doped carbon materials normally showed lower surface area [23], which were not for general use due to harsh reaction conditions, large metal nanoparticles and low catalytic activity. To overcome this shortcoming, mesoporous nitrogen-doped carbon materials have been explored by using a hard template strategy [24], usually with the help of HF or NaOH etching after nanocasting on mesoporous silica such as SBA-15. However, this process posed tremendous chemical handling challenges and led to environmental and manufacture cost issues.

In this work, we first synthesized the N-doped carbon material coated SBA-15 as the support of Ru species through a straightforward approach and then have attempted to employed these materials for catalytic hydrogenation of arenes and N-heterocycle compounds. That was, the N-doped carbon layer was immobilized onto the interior framework of SBA-15 utilizing a simple carbonization method, by which was to enhance Ru-support interaction of the catalytic composites. Subsequently, Ru species was introduced onto the support with an ultra-low Ru loading (*ca.* 0.1 wt.%). The sub-1-nm size Ru particles were obtained and anchored on CN-SBA-15 by a facile and efficient strategy. The optimal Ru/CN-SBA-15 catalyst exhibited a remarkably high TOF values and also excellent catalytic stability even if the reaction was carried out under the elevated temperature (around 100 °C) and aqueous phase conditions.

2. Experimental

2.1. Materials

All chemicals and solvents were commercially available and used as received without further purification. Ruthenium(III) chloride ($\text{RuCl}_3 \cdot n\text{H}_2\text{O}$, Ru, 37.01%), glucose (D-glucose anhydrous) and melamine were purchased by Sinopharm Chemical Reagent Co. Ltd. Hydrochloric acid (fuming, 37.00% solution in water), tetraethyl orthosilicate (TEOS, 98.00%), ethanol (Anhydrous 99.99%), pluronic P123 and all the substrates including Phenyl benzyl ether (BPE) were purchased from Aladdin. Co. Ltd. High purity N_2 (99.99%) and H_2 (99.99%) were supplied by Shang Nong Gas Factory. Commercial Ru/AC (5 wt.%) was obtained from Sino pharm Chemical Reagent Co. Ltd. The water used in all experiments was ultrapure.

2.2. Catalyst preparation

2.2.1. Preparation of CN-SBA-15

SBA-15 was synthesized according to the previous report (The details for the synthesis of SBA-15 were given in supporting information) [25]. The N-doped carbon layer coated SBA-15 were synthesized using the following procedure. 0.1 g melamine and 0.5 g glucose were dissolved in deionized water and then 0.5 g SBA-15 was added into the mixture. The resulting aqueous suspension was stirred in an open evaporating dish at 50 °C until the water was evaporated and a white solid was obtained. The white solid was ground, transferred into a quartz boat, followed by pyrolyzing in a quartz tube in a tube furnace under high purity nitrogen flow at 550 °C for 4 h with a ramp rate of 2.5 °C·min⁻¹. The nitrogen doped carbon layer coated SBA-15 was denoted as CN-SBA-15, where the content of nitrogen was found to be 3.96 wt.%. The other N-doping samples were denoted as CN-SBA-15-x, where x represented the percentage of nitrogen contents in the samples (x%=1.32%, 2.68% and 5.21%, respectively). While carbon layer coated SBA-15 was synthesized in a similar method without melamine and denoted as C-SBA-15. The sole carbon (C) or nitrogen-doped carbon (CN) was also prepared by carbonizing glucose or glucose and melamine directly at 550 °C without the addition of SBA-15.

2.2.2. Typical procedure for the preparation of the supported Ru catalysts

The supported Ru catalysts were prepared by the conventional incipient wetness impregnation. CN-SBA-15 was added to 8.0 mL ethanol with three drops of hydrochloric acid. And then 2.0 mL ethanol solution of RuCl₃ (0.7 mg/mL) was added the above solution under vigorous stirring. After continuous stirring vigorously at 50 °C about 12 h, the solvent was removed by evaporation at 80 °C, yielding a solid powder. The as-prepared powder was transferred into a crucible and then placed into a quartz tube furnace maintaining 250 °C for 2 h under flowing H₂ atmosphere with a heating rate of 2.5 °C min⁻¹ prior to the catalytic test. The resulting Ru (*ca.* 0.1 wt.%) catalyst was denoted as Ru/CN-SBA-15. Additionally, Ru/CN-SBA-15-x, Ru/C-SBA-15, Ru/SBA-15, Ru/C and Ru/CN were synthesized in a similar method.

2.3. Catalyst characterization

Powder X-ray diffraction (XRD) analysis of types samples were collected on a an Rigaku D/MAX 2550 VB/PC instrument equipped with a 9 kW rotating anode Cu source at 45 kV and 100 mA ($0.5-5^\circ$ and $5-75^\circ$, 0.2° s^{-1}). Raman spectroscopy was performed using a Thermo Scientific DXR Raman microscope. Raman Microprobe equipped with a 532 nm laser excitation source operated at 25 mW. Quanta chrome NOVA 2200e equipment was used to perform BET surface area analysis at -196°C with liquid nitrogen. Nitrogen physisorption was performed after degassing at 200°C for 5h to a vacuum of 10^{-3} Torr before analysis. The pore volume was reported at a relative pressure of 0.98. The pore size distribution from the adsorption isotherm was calculated by the BJH method. Thermo Scientific ESCALAB 250 was used to perform X-ray photoelectron spectroscopy (XPS) analysis. Field emission scanning electron microscopy (FESEM) images were performed on JSM electron microscopes (JEOL JSM-6360LV, Japan). High resolution transmission electron microscopy (HRTEM) was performed on a Tecnai G220 S-Twin transmission electron microscope with high-resolution option (200 kV). And high angle annular dark field scanning TEM (HAADF-STEM) was performed on a JEOL JEM 2010 transmission electron microscope operating at 200 kV with a nominal resolution of 0.2 nm. At least 150 Ru particles were counted for particle size distribution analysis. The samples for HRTEM and HAADF were prepared by dropping the ethanol solutions containing the NPs onto the holey carbon-coated Cu grids. FT-IR spectra were recorded from pressed KBr pellets at room temperature on a Nicolet Fourier transform infrared spectrometer (Magna550). A spectrum of dry KBr was also recorded as background. A CHNS elemental analyzer (Vario MICRO cube) was used to perform elemental analysis. The inductively coupled plasma atomic emission spectroscopy (ICP-AES) analysis was carried out on a Varian ICP-710ES instrument. The sample was putted in a plastic beaker mixed with a certain amount of aqua regia at 110°C for 6 h to dissolve the sample easily, followed by diluted with water. Static water contact angle (WCA) was carried out by the Contact Angle Meter (CA100C, Innuo Company, Shanghai, China) using the droplet profile as a method. The CA was determined using a tangent placed at the intersection of the liquid

and solid. A water droplet with a volume of 2 μL was dispensed by a piezo doser onto each sample disk. CO chemisorption was carried out on a Micromeritics AutoChem II 2920 system at 40 $^{\circ}\text{C}$ after in-situ reduction in H_2 at 400 $^{\circ}\text{C}$ for 1 h and flushing with helium at 200 $^{\circ}\text{C}$ for 0.5 h to remove any adsorbed H_2 . A chemisorption stoichiometry $\text{CO}/\text{Ru} = 1:1$ was used for calculation of Ru dispersion [26].

2.4. Catalytic reactions

The hydrogenation reaction was performed in a high-pressure batch autoclave of stainless steel with a 20 mL polytetrafluoroethylene liner. The autoclave was equipped with gas supply system and a magnetic stirrer. In a typical procedure, a certain amount of catalyst was dispersed in water, and then put into a certain amount of substrate. After purged with hydrogen for three times. The autoclave was sealed with the required hydrogen pressure and heated to the specified temperature in 25 minutes. Not counting until the set temperature was reached. After the reaction was finished, the reactor was quenched in an ice-water bath to stop the reaction. Straight after, the catalyst was filtrated to separate from the solution, the products in aqueous solution were extracted by diethyl ether several times and analyzed by GC and MS on Shimadzu GC-2014 equipped with an KB-50 MS (30 m long, 0.32 mm i.d., 0.50 μm film thickness) and an Agilent 6890/5973 GC-MS system equipped with a HP-5MS column (30 m long, 0.25 mm i.d., 0.25 μm film thickness) using *n*-butanol as the internal standard. The conversion of substrates and yield towards products were calculated as follows:

$$\text{Conversion (\%)} = \frac{\text{amount of substrates converted (mole)}}{\text{total amount of substrates (mole)}} \times 100\% \quad (1)$$

$$\text{Yield (\%)} = \frac{\text{amount of a product (mole)}}{\text{total amount of substrates (mole)}} \times 100\% \quad (2)$$

The turnover frequency TOF (h^{-1}) values were calculated on the basis of the total number of Ru atoms (bulk Ru) due to the surface supported subnanometer-scale Ru particles, unless otherwise indicated. The TOF (h^{-1}) was calculated by following Eq. (3) [27]:

$$\text{TOF (\text{h}^{-1})} = [(\text{reacted mol substrate})]/[(\text{total mol metal}) \times (\text{reaction time})] \quad (3)$$

In order to rule out other factors determining the activity (e.g. decrease of reactant

concentration or Ru sintering), the initial reaction rate was adopted (conversion was less than 15%).

The hydrogenation of BPE and pyridine were used for evaluating the recyclability of catalysts. Briefly, the hydrogenation of BPE was operated in a high-pressure batch autoclave of stainless steel. After reaction, the catalyst was washed with ethanol and water several times to remove the products, followed by drying at 60 °C for 10 h. Then the dried catalyst was used for the next run until operating eight runs. The recyclability of catalyst in pyridine hydrogenation was also carried out according to a similar procedure.

3. Results and Discussion

3.1. Catalyst characterization

The support and Ru nanoparticles have been believed to affect both activity and selectivity dramatically in hydrogenation reaction. However, the immobilization of the subnanosized Ru particles (<1nm) on supports has given a huge challenge. In this work, we have attempted to deposit a thin carbon or N-doped carbon layer on SBA-15, followed by loading ultra-low Ru (*ca.* 0.1 wt.%) on the support. Meanwhile, the present approach provides an effective approach to construct the ultra-fine Ru particles (0.2-0.7nm) by using a cheap RuCl₃ as a precursor. As shown in Table S1, the C, H and N contents of the as-prepared catalysts have been determined by elemental analysis and the Ru loading by ICP-AES, respectively.

The small-angle and wide-angle XRD patterns (Inset) was shown for the Ru catalysts in Fig. 1a. As shown from small-angle XRD patterns, the samples presented an intense (100) reflection at $2\theta = 0.5-1.1^\circ$ and two less intense (110) and (200) reflections at higher $2\theta = 1.3-2.1^\circ$, which were characteristic of the hexagonal *p6mm* symmetry of SBA-15 [28]. These results indicated that the porous structure of SBA-15 remained unchanged irrespective of the formation of Ru-based catalysts even with doping of carbon and nitrogen. However, the (100), (110) and (200) diffraction peaks of Ru/C-SBA-15 and Ru/CN-SBA-15 shifted to higher angle in comparison with that of sole SBA-15, especially the latter shifted to a larger extent, which was probably

because of the incorporation of carbon and nitrogen within the mesopore of SBA-15. Next, the wide angle XRD patterns were also presented in Fig. 1a (Insert), it could be seen that both Ru/C and Ru/CN samples showed two broad diffraction peaks at $\sim 24^\circ$ and 43° corresponding to the (002) and (100) diffraction planes, respectively [29]. The high intensity peak of the (002) plane could be ascribed to the average stack height of the aromatic planes of carbon crystallite and the peak of the (100) plane was attributed to the 2D graphitic structures [30]. Moreover, the low-intensity (002) and (100) diffraction peaks of Ru/C and Ru/CN indicated the relatively low degree of graphitization and amorphous structure of the samples [31]. On the other hand, from the wide angle XRD patterns, the Ru/SBA-15, Ru/C-SBA-15 and Ru/CN-SBA-15 catalysts showed a broad diffraction peak at $2\theta = 23.0^\circ$ that was assigned to the amorphous silica, while the peak at 24° and 43° assigned to carbon structures were almost indiscernible due to the low content of carbon materials on the SBA-15. Notably, only diffraction peaks arisen from the support appeared, but no diffraction peak assignable to Ru crystalline was observed in the wide-angle XRD patterns (Fig. 1a), implying that the Ru species were finely dispersed, with crystalline sizes below the XRD detection limit [32].

Raman spectroscopy was very sensitive to subtle structural variations in carbon materials, and thus the carbon materials or carbon layer coated SBA-15 supported Ru catalysts were characterized by Raman spectroscopy. As shown in Fig. 1b, it could be seen that both the D-band and the G-band arisen from Raman characteristic bands of carbon layer have been observed at 1350 cm^{-1} and $1578\text{-}1592\text{ cm}^{-1}$, respectively. The D-band represented the defect of the C atomic lattice, while the G-band corresponded to the in-plane stretching vibration of the C atom sp^2 hybridization [33]. The structural defects were caused by the impregnation of nitrogen, oxygen, metals and other impurities. Moreover, the relative intensities of the D-band (I_D) and G-band (I_G) provided the evidence for the characteristics of the carbon materials and the ratio I_D/I_G reflected the degree of graphitization. As shown from Fig. 1b, the ratio I_D/I_G for Ru/CN (0.88) was obviously higher than that of Ru/C ($I_D/I_G=0.69$), indicating that N-doping in the graphitic carbon layers resulted in reducing the degree of graphitization [34].

Simultaneously, this phenomenon was conserved basically between Ru/C-SBA-15 and Ru/CN-SBA-15. Notably, N-doping caused a downshift of the G band from 1592 cm^{-1} to 1578 cm^{-1} (Fig. 1b), which suggested substitution of nitrogen atoms within the graphitic network [35]. In addition, a very broad second-order (2D) band was observed at approximately 2725 cm^{-1} for Ru/C-SBA-15 and Ru/CN-SBA-15, reflecting that the existence of the broad 2D bands (more specifically the absence of a typical graphite shoulder) were characteristic features of few-layered graphene [36].

< Insert Fig. 1 >

Next, the texture of catalysts was investigated by the nitrogen adsorption-desorption measurements. Fig. S1 depicted the nitrogen adsorption-desorption isotherms and pore size distribution of the Ru catalysts. The corresponding textural properties (BET surface area, total pore volume and pore diameter) were summarized in Table 1. Ru/C and Ru/CN catalysts showed low BET surface area and poor porosity due to the absence of hard template reagent (SBA-15) (Table 1, entries 1 and 2) [37]. It could be observed from Fig. S1a that Ru/SBA-15 displayed a IV-type isotherm with an H1 hysteresis loop at the relative pressure between about 0.6 and 0.8, indicating that it was mesoporous with relatively uniform mesoporous size centered at 8.2 nm (Fig. S1a, insert). Ru/C-SBA-15 also showed a similar N_2 adsorption-desorption isotherm and mesoporous properties with an average pore size of around 7.5 nm (Fig. S1b, insert). The smaller average pore size with respect to SBA-15 resulted from the carbon coated on the pore surface of silica as well as shrinkage of silica which could occur at high temperatures [38]. Similarly, Ru/CN-SBA-15 also exhibited the uniform and ordered cylindrical mesopore despite the nitrogen doping. The pore size slightly declined to 7.0 nm (Table 1, entry 7). Meanwhile, the BET surface area decrease from $757\text{ m}^2\text{ g}^{-1}$ to $498\text{ m}^2\text{ g}^{-1}$ and pore volume from $1.139\text{ cm}^3\text{ g}^{-1}$ to $0.556\text{ cm}^3\text{ g}^{-1}$ respectively, owing to the N-doped carbon layer coated on SBA-15. Moreover, nitrogen adsorption-desorption isotherms and pore size distribution of the Ru catalysts with different N-doping contents have also been given in Fig. S2. The corresponding textural properties

of Ru/CN-SBA-15-x catalysts were listed in Table 1 (Entries 5, 6 and 8). It can be observed that BET surface area, total pore volume and pore diameter of Ru/CN-SBA-15-x decreased with the increase of nitrogen content. Especially for Ru/CN-SBA-15-5.21, BET surface area, total pore volume and pore diameter declined to $381 \text{ m}^2 \text{ g}^{-1}$, $0.405 \text{ cm}^3 \text{ g}^{-1}$ and 5.2 nm respectively. This indicated that increasing the nitrogen doping on the support could cause a dramatic shrinkage of the mesopores.

<Insert Table 1>

The nature of the doped N atoms in these samples was assessed by X-ray photoelectron spectroscopy (XPS) (Fig. 2), and the spectra were calibrated using silicon at 103.4 eV . It could be observed that C 1s spectra of Ru/C-SBA-15 exhibited three deconvoluted binding energy peaks: the strong peak at 284.4 eV was ascribed to the aromatic carbon (sp^2 carbon), the peak at 285.6 eV corresponded to the aliphatic carbon (sp^3 carbon) and the peak at 286.8 eV was ascribed to carbonyl ($\text{C}=\text{O}$), respectively (Fig. 2a) [39]. Subsequently, Fig. 2b showed the C 1s XPS of Ru/CN-SBA-15, in which C 1s revealed almost a similar set of binding energy peaks as that of Ru/C-SBA-15 except $\text{sp}^3 \text{ C}-\text{N}$ as observed at 287.5 eV and $\text{sp}^2 \text{ C}=\text{N}$ at 285.6 eV . This result implied that the carbon framework of the resulting Ru/CN-SBA-15 was successfully doped with N heteroatoms [40]. Additionally, the high resolution N 1s spectrum of CN-SBA-15 (Fig. 2d) could be deconvoluted into four individual peaks, which was assigned to pyridinic-N at 398.2 eV , pyrrolic-N at 399.9 eV , quaternary-N at 400.7 eV and oxidized-N at 402.0 eV , respectively [41]. Meanwhile, N 1s spectrum of Ru/CN-SBA-15 (Fig. 2c) also exhibited four different peaks associated with the different nitrogen states of pyridinic-N (398.9 eV), pyrrolic-N (400.0 eV), quaternary-N (400.9 eV) and oxidized-N (402.1 eV). Notably, the binding energies of the pyridinic-N of Ru/CN-SBA-15 were shifted to high values due to the introduction of Ru, which moved from 398.2 eV to 398.9 eV (Fig. 2c vs 2d). This demonstrated clearly that pyridinic-N could be preferentially bound to the Ru particles, leading to electron transfer from these N atoms to Ru.

< Insert Fig. 2 >

As shown in Fig. 3, the high resolution XPS spectra of Ru 3p revealed the surface characteristics of the Ru species, and the spectra were calibrated using carbon at 284.4 eV. The main peak of Ru 3p 3/2 around 462 eV corresponded to zero-valent Ru, and the peak around 465 eV could represent high-valent Ru(n^+) [42]. Among the three catalysts, Ru/CN-SBA-15 presented the greatest percentage of Ru(0) (96%), as compared with that of Ru(0) (88%) in Ru/C-SBA-15 and Ru(0) (86%) in Ru/SBA-15. In addition, the surface Ru particles were in an electron-poor state as compared with the nitrogen species. If the interaction existed between the Ru and nitrogen atoms through the lone electron pair or π -electrons of nitrogenous functional groups resulting from sp^2 hybridization, the electron transfer occurred between the nitrogen and Ru atoms, the binding energy of the surface Ru atoms would shift to a lower value [43]. As expected, the Ru 3p 3/2 binding energy of Ru/CN-SBA-15 indeed moved toward lower value significantly (461.6 and 464.7 eV), as compared with those of the Ru-SBA-15 and Ru/C-SBA-15 (462.3 and 465.1 eV). It suggested that the doped nitrogen atoms in the carbon layer donated electron density to active Ru sites on the support, which was in well agreement with that of the N 1s spectra above (Fig. 2). Hence, the incorporation of nitrogen in the carbon carrier resulted in increasing proportions of Ru(0) due to the electron donating effects of nitrogen.

< Insert Fig. 3 >

Based on the above characterization of XRD, Raman, porosity and XPS, it indicated that a large amount of N atoms were doped in the carbon layers and the Ru species were preferentially bound to pyridinic-N atoms. However, the morphology of carbon, nitrogen doped carbon or N-doped carbon coated SBA-15 supports was still not clear. Subsequently, the surface morphology of all catalysts was examined by FESEM. As shown in Fig. 4b and 4c, both Ru/C and Ru/CN revealed irregular petal-like

appearance due to the partial disorder of the carbon layer. By contrast, SBA-15 displayed a uniformly fibrous macroscopic structure with relatively uniform size of 200-400 nm (Fig. 4a). Notably, the catalysts such as Ru/SBA-15, Ru/C-SBA-15 and Ru/CN-SBA-15 also showed no obvious changes of morphology, as compared with that of parent SBA-15 even if the incorporation of carbon layer and Ru species (Fig. 4d-4f). Similarly, all these samples exhibited the rope-like units with the diameter in the range of 200-500 nm, which was in good agreement with the previous report [24].

< Insert Fig. 4 >

To identify the effect of the different supports on the sizes of Ru particles, high resolution transmission electron microscopy (HRTEM) was carried out from Fig. S3. Unfortunately, there were no obvious Ru nanoparticles as discerned in the images of HRTEM, revealing that Ru particles may be existed in subnanosized scale. However, the highly order array of pore channels of Ru/CN-SBA-15 catalyst could be discerned clearly. Sequentially, typical high-angle annular dark-field scanning TEM (HAADF-STEM) has been applied for characterization of the Ru-based catalysts. Fig. 5 displayed the images and the particle size distribution of Ru nanoparticles supported on various supports. Meanwhile, the mean sizes of Ru particles have also been listed in Table 1.

As shown in Fig. 5a, Ru particles on carbon support (Ru/C) had a serious aggregates and uneven distribution owing to poor BET surface area and weak interaction between carbon and Ru species. Nevertheless, once adding nitrogen (Ru/CN), the degree of aggregation with Ru was greatly reduced and Ru nanoparticle size decreased to 3 nm (Fig. 5b) compared to that of Ru/C (5 nm). Moreover, SBA-15 with the ordered mesoporous structure and large BET surface area promised that Ru species was homogeneously dispersed on the pore channels and the mean size of Ru nanoparticle was observed to be around 1.2 nm (Fig. 5c). On the other hand, when SBA-15 was coated with carbon layer but without N-doping, the average size of Ru particles was about 1.7 nm and the size distribution was very broad despite the existence of uniform pore channels in Ru/C-SBA-15 (Fig. 5d). Interestingly, it was surprising to find

that the average particle size on Ru/CN-SBA-15 catalyst was only 0.5 nm. Simultaneously, the ultra-fine Ru particles had almost no aggregation and dispersed uniformly on the CN-SBA-15 support during the reduction process (Fig. 5e), likely resulting from the synergistic role of doping-N carbon layer and mesoporous SBA-15. As evidenced by XPS spectra, the strong interaction between the doped N atoms and Ru atoms could prevent the subnanosized Ru particles from the aggregation in the course of catalyst preparation. Meanwhile, the corresponding energy-dispersive X-ray spectroscopy (EDS) of the selected areas observed in HAADF-STEM images of the Ru-CN/SBA-15 catalyst, showing the presence of Ru signals.

< Insert Fig. 5 >

To get insight into the effect of the N-doping contents on the size of Ru particles, HAADF-STEM has also been applied for the characterization of the Ru/CN-SBA-15-x catalysts. From Fig. S4 and Fig. 5e, it could be seen that the Ru particles were homogeneously dispersed on all N-doped SBA-15 supports. Additionally, the size of Ru particles decreased from 1.1 nm to 0.5 nm when the nitrogen contents increased from 1.32 to 3.96 wt.% (Table 1, entries 5-8). However, when the nitrogen contents continued to increase up to 5.21 wt.%, the size of Ru particles became larger and was up to 1.4 nm. These results above indicated that the introduction of nitrogen did enhance the interaction between support and Ru, thereby promoting the dispersion and stability of Ru nanoparticles. Nevertheless, an excess of nitrogen contents would result in a remarkable shrinkage of the mesopores (Table 1, entry 8), which might cause the aggregation of Ru nanoparticles.

3.2. Hydrogenation reaction in aqueous phase

The hydrogenation reaction has been performed in aqueous phase because water is certainly a green solvent and also allowed easy separation of products and recycling of the catalyst. The toluene hydrogenation was used as a relevant benchmark reaction over all Ru-based catalysts. This reaction was typically operated in water at 100 °C and

2.0 MPa H₂ (Table 2). The blank test showed that the reaction did not happen without catalysts (Table 2, entry 1). Similarly, Ru-free materials like C-SBA-15 and CN-SBA-15 also showed no activity (Table 2, entries 2 and 3). However, once a small amount of Ru (*ca.* 0.1 wt.%) was introduced to the supports, the resultant Ru-based catalysts became active for the hydrogenation and the catalytic activities were highly dependent on the properties of the supports and Ru particles (Table 2, entries 4-8).

Ru/C catalyst showed low activity for toluene hydrogenation even with a long reaction time (Table 2, entry 4). It was observed visually that the Ru/C catalyst was highly hydrophobic, which caused the catalyst not to disperse well in the aqueous solution and the catalyst precipitated immediately once the stirring stopped, thus preventing the Ru catalyst from a sufficient contact with the substrate. In addition, the poor BET surface area (<10 m² g⁻¹) and larger Ru particles (5.0 nm) could also have negative impacts on catalytic performance. Unfortunately, the N-doped carbon material immobilizing Ru showed only a slightly higher catalytic activity than that of Ru/C (Table 2, entry 4 *vs* 5), although the aqueous dispersion of the Ru catalyst was improved to some degree by visual observation. However, Ru/CN still exhibited hydrophobic property due to a large WCA (120°) (Fig. S5a). On the contrary, Ru/SBA-15 have shown excellent catalytic activity and TOF value could reach up to 5072 h⁻¹ (Table 2, entry 6), assigning to BET surface, the regular channel structure, smaller Ru nanoparticles and strong hydrophilic property (WCA=0°, Fig. S5b). It has been reported previously that the encapsulation of metal nanoparticles into the mesoporous SBA-15 could effectively prevent the coalescence of Ru due to the confinement effects and also provide wide channels for the reactants to reach the surface of metal Ru, thus allowing catalytic reaction to occur [44]. However, Ru/C-SBA-15 afforded TOF up to 4026 h⁻¹ (Table 2, entry 7), which was slightly lower than that of Ru/SBA-15. This could result from decreasing BET surface area, pore size (Table 1, entry 3 *vs* 4), and also hydrophilicity (Fig. S5c *vs* S5b), as compared with that of Ru/SBA-15, and also an aggregation of Ru particles to some extent, as reflected by the images of HAADF-STEM (Fig. 5c *vs* 5d).

Notably, as shown in Table 2, the Ru/CN-SBA-15 catalyst exhibited the highest

catalytic activity for catalytic hydrogenation of toluene into methylcyclohexane and TOF increased up to 7289 h^{-1} (Table 2, entry 8) even if BET surface area was lower, as compared with Ru/SBA-15 and Ru/C-SBA-15 (Table 1, entries 3 and 4 vs 5). This demonstrated clearly that the N-doped carbon layer coated on the SBA-15 played a crucial role in enhancing the hydrogenation activity. First, the electron transfer induced the deletion of electron density in the doped N atoms, enriching the electron density of Ru nanoparticles and thus enhancing their catalytic activities remarkably [43,45]. Second, the strong interaction between basic nitrogen atoms and Ru species enormously promoted the excellent dispersion of the subnanosized Ru particles (Fig. 5e). Third, the synergistic effects of N-doping carbon material and SBA-15 provided a relatively large BET surface area compared to Ru/C and Ru/CN (Table 1), which would make significant contribution to generating much more exposed active sites on the surface of catalysts, allowing substrates to diffuse to the active sites with relatively less barriers. Besides, N-doped carbon layer slightly increased hydrophilicity of the Ru catalyst (Fig. S5c vs S5d), and then enhanced the dispersion of catalysts in aqueous phase, which could promote toluene to adsorb on the active site and be hydrogenated more easily [20]. Meanwhile, we found that N-doped contents did have a significant effect on the catalytic performance (Fig. S6). The catalytic activity was highly relevant to the size of Ru particles. For example, Ru/CN-SBA-15 showed the highest catalytic activity when the nitrogen contents were adjusted to 3.96 wt.% (Fig. S6) due to the smallest Ru nanoparticles on Ru/CN-SBA-15-x catalysts (Table 1, entries 5-8), which would allow more Ru atoms exposed on the particle surface. Next, to examine the intrinsic activity of all Ru-based catalysts, the Ru loading was increased to 1.0 wt.% in order to ensure the more accurate measurement of CO chemisorption and thus Ru dispersion can be given accordingly. As shown in Table S2, the Ru/CN-SBA-15 catalyst gave the highest TOF values even if the Ru sites exposed on the surface was adopted, indicating the N-doping materials indeed endowed the Ru-based catalysts with higher the intrinsic activity.

For the sake of comparison, a standard commercially available Ru/AC catalyst was evaluated for toluene hydrogenation and displayed only moderate activity and the

TOF was only 294 h^{-1} (Table 2, entry 9), revealing that the present Ru/CN-SBA-15 catalyst exhibited about 21 times higher catalytic activity than that of the commercial Ru/AC catalyst. Actually, the TOF values on Ru/CN-SBA-15 catalyst was also much higher than those reported aqueous-phase catalyst systems in hydrogenation of aromatics [46-48]. Hence, the Ru/CN-SBA-15 catalyst provided an attractive pathway to maximize the usage of the precious Ru in green aqueous media.

< Insert Table 2 >

Fig. 6 displayed the correlation between the TOF values and the sizes of the supported Ru particles derived from Fig. 5. It could be seen distinctly that TOF values increased very slowly at the size of Ru ranged from 5.0 nm to 3.0 nm. Interestingly, the TOF values raised sharply as the size of Ru particles reduced from 3.0 nm to 0.5 nm. This enhancement of activity was not only associated with an increase on the numbers of the active Ru sites attributing to the presence of a larger proportion of Ru subnanoparticles, but also the electron-rich Ru sites. What's more, such an increasing trends of the TOF values seemed to be more distinct under the higher reaction temperature, indicating that the intrinsic activity of the small Ru particles is higher than that of the large Ru particles.

< Insert Fig. 6 >

To get a deep insight into the catalytic properties of Ru-based catalysts, the representative catalysts, i.e. Ru/SBA-15, Ru/C-SBA-15 and Ru/CN-SBA-15 were applied for further studies. The kinetic plots of toluene to methylcyclohexane conversion over these catalysts were shown in Fig. 7. Taking Ru/CN-SBA-15 as an example, excluding the interference of internal and external diffusion (Fig. S7), the relationship between the reaction rate [R_0 ; Eq. (4)] and the concentrations of substrate (toluene) was shown in Fig. S8, where the reaction order was then derived. The concentration of hydrogen was considered to be a constant since hydrogen was

excessive. The study showed a reasonable zero-order plot for the loss of concentration of toluene (0.36-0.90M), indicating a strong adsorption of the toluene on the surface of the catalysts [49]. Hence, we found that water contents had a little effect on hydrogenation of toluene (Table 2, entries 8). And then the reaction rate equation was showed by using Eq. (4) at a constant concentration of hydrogen, where R_0 and k represented the reaction rate and rate constant, respectively.

$$R_0 = - [d(\text{toluene})/dt] = k [\text{toluene}]^0 \quad (4)$$

The apparent activation energies of Ru catalysts, calculated from the Arrhenius equation, gradually increased in the following order: 31.82 kJ/mol (Ru/CN-SBA-15) < 36.89 KJ/mol (Ru/SBA-15) < 42.09 kJ/mol (Ru/C-SBA-15) (Fig. 7), which indicated that the apparent activation energies increased with the size of the Ru particles. This phenomenon was actually in agreement with that as shown in Fig. 6. Particularly, the apparent activation energies on Ru/CN-SBA-15 catalyst were much lower than that of the reported systems [49,50], which could be attributed to the unique properties of Ru subnanoparticles and the N-doped carbon materials could facilitate hydrogenation of arenes [51].

< Insert Fig. 7 >

The catalytic hydrogenation of Ru/CN-SBA-15 for olefins, arenes and the other biomass-derived platform molecules has been demonstrated in Table 3. Both alicyclic olefin and linear olefin (cyclohexene and 1-hexene) were highly reactive over the present catalyst under the aqueous and much more mild conditions, and even TOFs were over 10000 h⁻¹ (Table 3, entries 1 and 2). Moreover, the styrene was hydrogenated smoothly into ethylcyclohexane in 99% yield even under a reaction condition of 60 °C and TOF reached up to 8273 h⁻¹ (Table 3, entry 3). Similarly, the other arenes like phenylacetylene, toluene and *o*-xylene were also converted into the corresponding totally hydrogenated products respectively, although the complete hydrogenation of these substrate molecules could require slightly longer reaction time or higher temperature due to the electron-withdrawing substituent or the steric hindrance (Table

3, entries 4-6).

As we have known, a majority of the industrially important arene derivatives are produced from fossil fuel feedstock. However, the rapid depletion of fossil fuels necessitates a search for sustainable alternatives such as biomass whose valorization produces oxygenated aromatics [52]. Hence, hydrogenation of aromatic cores of lignin-derived compounds and other oxygenated aromatics are also indispensable chemical transformations. Herein, the Ru/CN-SBA-15 catalyst has been extended for the hydrogenation of the substrates containing oxygen group like phenols, aromatic alcohol, ketone, ester and ether (Table 3, entries 7-14). For instance, the phenol and its derivatives were all converted into the corresponding alicyclic reaction products almost stoichiometrically under very mild conditions (Table 3, entries 7-10). In particular, the presence of functional group such as methoxyl or hydroxyl groups did not affect consequence of the hydrogenation reaction, which afforded ideal yield of products (Table 3, entries 8-10). Furthermore, benzyl alcohol was easily hydrogenated to form cyclohexyl methanol under more mild conditions (Table 3, entry 11). Therewith, acetophenone was hydrogenated into 1-cyclohexylethan-1-ol with full conversion and 95% yield, and a trace of ethylcyclohexane was detected as a by-product possibly via the tandem consecutive dehydration and hydrogenation of 1-cyclohexylethan-1-ol (Table 3, entry 12). Notably, the hydrogenation of ethyl benzoate was complete and very selective within 7 h (Table 3, entry 13). Especially, in the hydrogenation of benzylic ethers, the cleavage of the C–O bond easily occurred, attributing to the lower C–O bonding dissociation energy. However, applying the present Ru/CN-SBA-15 catalyst gave excellent selectivity for the hydrogenation of the arene rings of phenyl benzyl ether without C-O bond cleavage, and thus alicyclic ether was achieved with 96% yield (Table 3, entry 14).

Next, the Ru/CN-SBA-15 catalyst was also employed for the hydrogenation of the other biomass-derived platform molecules. As shown in Table 3, both furfural and 5-hydroxymethylfurfural were converted almost stoichiometrically into tetrahydrofurfuryl alcohol and (tetrahydrofuran-2,5-diyl) dimethanol, respectively (Table 3, entries 15 and 16). Meanwhile, it indicated that for the hydrogenation of furfural (Fig. S9), the reaction

was not the zero-order, and an increase of water amount resulted in the decrease of activity due to the lower concentration of furfural likely due to the first order reaction [53]. Finally, we also examined the hydrogenation of levulinic acid with Ru/CN-SBA-15 catalyst, it could be seen that the catalyst also exhibited excellent activity with high TOF up to 4092 h^{-1} and γ -valerolactone was produced in excellent yield (Table 3, entry 17). As a whole, Ru/CN-SBA-15 exhibited good-to-excellent activity in the hydrogenation of arenes, phenols the biomass-derived molecules, particularly in the transformation of aromatics to the corresponding alicyclic compounds. The results above revealed clearly that Ru/CN-SBA-15 indeed showed much higher activity (TOF) than that of Ru/C-SBA-15 for all substrate hydrogenation (Table 3 vs Table S3), which elucidated that the N-doping support played an indispensable role in improving catalytic activity of Ru subnanoparticles.

<Insert Table 3>

It has been demonstrated that the selective hydrogenation of N-heteroarenes is a long-term scientific and technological challenge due to the high resonance stability of these substrates, and the potential poisoning of the metal catalysts owing to the coordination with nitrogen in either substrates or their reduced products [54]. Fortunately, attributing to the unique properties of Ru subnanoparticles endowed by the doped N atoms in carbon layer, promising Ru/CN-SBA-15 to show excellent ability for the efficient hydrogenation of N-heteroarenes. As shown in Table S4, the hydrogenation reaction of pyridine did not happen at all in the absence of Ru catalysts (Table S4, entries 1-3). The reaction proceeded very sluggishly with Ru/C, Ru/CN, Ru/SBA-15 and Ru/C-SBA-15 catalysts (Table S4, entries 4-7). The commercial Ru/AC catalyst actually also gave a similar activity to that of the Ru catalysts above (Table S4, entry 9). In contrast, on the optimal Ru/CN-SBA-15 catalyst, pyridine was successfully hydrogenated to piperidine in 99% yield in aqueous phase even under more mild conditions (Table S4, entry 8). These results demonstrated that a co-existence of N-doping carbon layer and SBA-15 was very crucial for the hydrogenation of N-

heteroarenes.

To showcase the applicability of this novel catalyst, the hydrogenation was utilized for the other N-heterocyclic compounds. As shown in Table 4, the hydrogenation of pyridine and 4-methylpyridine could afford the desired product in excellent yield without by-products (Table 4, entries 1 and 2) although the reactivity of 4-methylpyridine was somewhat less than that of pyridine, and a slightly longer reaction time (7.5 h) was needed for full conversion (Table 4, entry 2). Additionally, indole was entirely transformed to dihydroindole and quinoline was completely converted to 1,2,3,4-tetrahydroquinoline with high selectivity, respectively (Table 4, entries 3 and 4).

<Insert Table 4>

To identify the possible interaction between pyridine ring or pyrrole ring and N-doping carbon layer on SBA-15, the FTIR spectra of Ru/CN-SBA-15 and Ru/CN-SBA-15 catalyst adsorbed with quinoline were shown in Fig. 8. From Fig. 8a, the peak at 3236 cm^{-1} were assigned to N-H stretching vibration belonging to Ru/CN-SBA-15 [55]. As quinoline was adsorbed on the surface of the catalyst (Fig. 8b), the stretching vibration of N-H occurred redshift to 3227 cm^{-1} , which indicated the surface nitrogen atoms of N-doping carbon layer could interact with pyridinic-N of quinoline through forming the strong N-H...N hydrogen bonds, promoting the hydrogenation reaction and accounting for an excellent selectivity towards 1,2,3,4-tetrahydroquinoline [56]. Meanwhile, the formation of this hydrogen bond could activate substrate molecules and weaken the coordination of the nitrogen atoms in substrate/product with active metal species, which probably prevented active Ru sites from poisoning to some degree. Notably, the characteristic peaks of the benzene ring region ($1500\text{-}1650\text{ cm}^{-1}$) of quinoline adsorbed on Ru/CN-SBA-15 did not show any obvious changes compared to that of quinoline molecule, indicating that there was no apparent π - π interaction between quinoline and the surface carbon layer of the catalyst.

< Insert Fig. 8>

Next, the reusability of the catalysts was determined because catalysts recyclability exhibited an indispensable part in the economic evaluation of chemical compound transformations. Because Ru/C and Ru/CN exhibited very low hydrogenation activity, they were not subjected to the catalytic recycling. Here, the hydrogenation of BPE was applied as the model reaction under the optimal experimental conditions for the consecutive catalyst recycling (Fig. 9). As shown in Fig. 9a, Ru/SBA-15 catalyst showed a sharp deactivation for BPE hydrogenation after three cycles in spite of an excellent initial activity, while Ru/C-SBA-15 afforded much better recyclability (Fig. 9b) than that of Ru/SBA-15, but the yield of alicyclic ether decreased slowly during the consecutive runs. Particularly, Ru/CN-SBA-15 catalyst revealed the best recyclability and the decrease in yield of alicyclic ether was not obvious even the catalyst was subjected to recycling up to eight times in the aqueous phase (Fig. 9c). The first-rank catalyst was also showed the excellent recyclability in hydrogenation of pyridine into piperidine. As shown in Fig. S10, the activity did not changed significantly in the successive eight runs.

< Insert Fig. 9 >

The reused Ru catalysts for BPE hydrogenation have been characterized for the possible structural changes. As shown in Fig. S11, the ordered mesoporous silica structure collapsed completely for Ru/SBA-15 catalyst, while the coating carbon material layer on SBA-15 could enhance the stability greatly and the recycling test could not influence the ordered mesoporous silica structure of Ru/C-SBA-15 and Ru/CN-SBA-15. Furthermore, N₂ adsorption-desorption isotherms (Fig. S12) and pore size distribution of the spent Ru/SBA-15 Ru/C-SBA-15 and Ru/CN-SBA-15 catalysts (Table S5) have demonstrated that the carbon layer indeed gave contribution to greatly improving the stability of the supports. Compared to the previous research [57,58], the high content of carbon materials on SBA-15 can lead to a thicker layer of carbon, prevented the mesoporous SBA-15-based samples from collapse of the well-ordered

mesoporous structure even under the aqueous and high temperature reaction condition. Simultaneously, as seen from Fig. S13, the spent Ru/CN-SBA-15 catalyst displayed the percentage of Ru(0) (70%), which was slightly lower than that of the fresh Ru/CN-SBA-15, and thus demonstrating that although a fraction of the Ru(0) was transformed into Ru(n^+) in the course of catalytic recycles, no significant influence on catalytic activity was observed (Fig. 9c).

Then FESEM and HAADF-STEM was also operated for the further characterization of the used catalysts in BPE hydrogenation. Interestingly, as shown from the images of FESEM (Fig. 10a-10c), the reused Ru/SBA-15 catalyst showed an irregular and porous appearance, while the reused Ru/C-SBA-15 and Ru/CN-SBA-15 catalysts displayed the same uniformly fibrous macroscopic structure as that of the corresponding fresh catalysts (Fig. 4d-4f vs Fig. 10a-10c). These results actually were in well agreement with that of N_2 adsorption-desorption measurement (Table S4). Furthermore, the HAADF-STEM images of the spent catalyst could afford the size distribution of Ru particles. As shown in Fig. 10d-10f, Ru particles supported on SBA-15 aggregated seriously after recycling (Fig. 10d), and even no discernable Ru particles could be observed. Ru particles supported on C-SBA-15 easily sintered to form much bigger particles after consecutive runs, whose diameter increased from 1.7 nm to 3.0 nm (Fig. 5d vs Fig. 10e) although the mesoporous structure was not destroyed (Fig. S6). Notably, the Ru particles on CN-SBA-15 were still well-dispersed, with the average Ru particle diameter increasing slightly, from 0.5 nm to 0.8 nm (Fig. 5e vs Fig. 10f). Moreover, ICP analysis proved that the leaching of Ru species on Ru/CN-SBA-15 catalyst was negligible (3.4%) in the course of the consecutive runs (Table S1, entry 5), as compared with that of Ru/SBA-15 and Ru/C-SBA-15 catalysts (Table S1, entries 3 and 4). This further proved that the Ru particles were robustly anchored to nitrogen functional groups and the interaction between the nitrogen and Ru species could effectively prevented the aggregation and leaching of the Ru subnanoparticles.

< Insert Fig. 10 >

4. Conclusions

In summary, we have demonstrated a simple and versatile method to construct highly active heterogeneous Ru catalysts. This catalyst shows high catalytic activity and excellent recyclability for the selective hydrogenation of arenes, phenols and N-heteroarenes into the corresponding alicyclic compounds under relatively mild reaction conditions, which can be mainly attributed to the positive synergistic effect between the N-doped carbon layer coating and the sub-1-nm size Ru particles. It can be found that carbon coatings can improved hydrothermal stability to mesoporous structural SBA-15, and the N-doped carbon layers on SBA-15 helped to better disperse and stabilize the Ru sub-nanoparticles compared to the sole carbon layers. The Ru particles was preferentially dispersed on the pyridine-type nitrogen sites, leading to an electron transfer from nitrogen atoms to active Ru sites. Moreover, pyridinic-N of quinoline molecules showed the interaction with the doped N atoms through forming the strong N-H...N hydrogen bonds, which results in the strong adoption and higher reactivity. Especially, the TOF values raised sharply with the decreasing size of Ru particles in the range of 0.5 nm to 3.0 nm. Overall, the present strategy provided a very effective way to prevent the leaching or aggregation of ultra-fine Ru particles even under aqueous reaction conditions, and may allow us to maximize the efficient usage of the precious Ru for a variety of sustainable technology applications.

Acknowledgements

The authors are grateful for financial support from the National Natural Science Foundation of China (21622305, 21773061), the innovation Program of Shanghai Municipal Education Commission (15ZZ031), the Fundamental Research Funds for the Central Universities.

References

- [1] C.H. Pélisson, A. Denicourt-Nowicki, A. Roucoux, *ACS Sustainable Chem. Eng.* 4 (2016) 1834-1839.
- [2] T. Ouchi, C. Battilocchio, J.M. Hawkins, S. V. Ley, *Org. Process Res. Dev.* 18 (2014)

- 1560-1566.
- [3] S. Källström, R. Leino, *Bioorg. Med. Chem.* 16 (2008) 601-635.
- [4] D.S. Wang, Q.A. Chen, S.M. Lu, Y.G. Zhou, *Chem. Rev.* 113 (2011) 2557-2590.
- [5] F. Meemken, A. Baiker, *Chem. Rev.* 117 (2017) 11522-11569.
- [6] X. Li, B.N. Popov, T. Kawahara, H. Yanagi, *J. Power Sources* 196 (2011) 1717-1722.
- [7] A.B. Ayusheev, O.P. Taran, I.A. Seryak, O.Y. Podyacheva, *Appl. Catal. B* 146 (2014) 177-185.
- [8] L. Liu, A. Corma, *Chem. Rev.* 118 (2018) 4981-5079.
- [9] J.J. Li, W. Chen, H. Zhao, X.S. Zheng, L.H. Wu, H.B. Pan, J.F. Zhu, Y.X. Chen, J.L. Lu, *J. Catal.* 325 (2017) 371-381.
- [10] T. Koh, H.M. Koo, T. Yu, B. Lim, J.W. Bae, *ACS Catal.* 4 (2014,) 1054-1060.
- [11] S. Ghosh, B.R. Jagirdar, *ChemCatChem* 10 (2018) 3086-3095.
- [12] P. Lara, K. Philippot, B. Chaudret, *ChemCatChem* 5 (2013) 28-45.
- [13] J.F. Wang, J.A. Chen, P.F. Wang, J. Hou, C. Wang, Y.H. Ao, *Appl. Catal. B* 239 (2018) 578-585.
- [14] M. Ruta, N. Semagina, L. Kiwi-Minsker, *J. Phys. Chem. C* 112 (2008) 13635-13641.
- [15] M. Takasaki, Y. Motoyama, K. Higashi, S.H. Yoon, I. Mochida, H. Nagashima, *Chem-Asia. J.* 2 (2007) 1524-1533.
- [16] H. N. Pham, A.E. Anderson, R.L. Johnson, K. Schmidt-Rohr, A.K. Datye, *Angew. Chem. Int. Ed.* 51 (2012) 13163-13167.
- [17] D.W. Gardner, J.J. Huo, T.C. Hoff, R.L. Johnson, B.H. Shanks, J.P. Tessonnier, *ACS Catal.* 5 (2015) 4418-4422.
- [18] L.Q. Wu, J.L. Song, B.W. Zhou, T.B. Wu, T. Jiang, B.X. Han, *Chem-Asia. J.* 11 (2016) 2792-2796.
- [19] Y.H. Hu, G.C. Jiang, G.Q. Xu, X.D. Mu, *Mol. Catal.* 445 (2018) 316-326.
- [20] D.H. Tang, X. Sun, D. Zhao, J.J. Zhu, W.T. Zhang, X.L. Xu, Z. Zhao, *ChemCatChem* 10 (2018) 1291-1299.
- [21] L. He, F. Weniger, H. Neumann, M. Beller, *Angew. Chem. Int. Ed.* 55 (2016)

- 12582-12594.
- [22] Y.F. Yang, L.T. Jia, B. Hou, D.B. Li, J.G. Wang, Y.H. Sun, *ChemCatChem* 6 (2014) 319-327.
- [23] X.F. Chen, L.G. Zhang, B. Zhang, X.C. Guo, X.D. Mu, *Sci. Rep.* 6 (2016) 28558.
- [24] Y.T. Gong, P. F. Zhang, X. Xu, Y. Li, H.R. Li, Y. Wang, *J. Catal.* 297 (2013) 272-280.
- [25] H.L. Chiang, T.N. Wu, L.X. Zeng, *Microporous Mesoporous Mater.* 279 (2019) 286-292.
- [26] A. Philippaerts, S. Goossens, W. Vermandel, W. Vermandel, M. Tromp, *ChemSusChem* 4,6 (2011) 757-767.
- [27] P. F. Zhang, Y.T. Gong, H.R. Li, Z.R. Chen, Y. Wang, *Nat. Commun.* 4 (2013) 1593.
- [28] X.C. Cai, Y.Q. Wang, J.Y. Liu, Z.Y. Xie, Y. Long, J. Zhou, J. Wang, *ACS Sustainable Chem. Eng.* 4 (2016) 4986-4996.
- [29] P. Puthiaraj, K. Kim, W.S. Ahn, *Catal. Today* 324 (2019) 49-58.
- [30] S.Y. Tao, Y.C. Wang, D. Shi, Y.L. An, J.S. Qiu, Y.S. Zhao, Y. Gao, X.F. Zhang, *J. Mater. Chem. A* 2 (2014) 12785-12791.
- [31] K.X. Xiang, S.Y. Cai, X.Y. Wang, M.F. Chen, S.X. Jiang, *J. Alloys Compd.* 740 (2018) 687-694.
- [32] Z.Y. Zhang, L.P. Ding, J. Gu, Y.L. Li, N.H. Xue, L.M. Peng, Y. Zhu, W.P. Ding, *Catal. Sci. Technol.* 7 (2017) 5953-5963.
- [33] S.M. Lyth, W. Ma, J. Liu, T. Daio, K. Sasaki, A. Takahara, B. Ameduri, *Nanoscale* 7 (2015) 16087-16093.
- [34] A. Choudhury, J.H. Kim, M.S. Sinha, K.S. Yang, D. J. Yang, *ACS Sustainable Chem. Eng.* 5 (2017) 2109-2118.
- [35] D.C. Wei, Y.Q. Liu, Y. Wang, H.L. Zhang, L.P. Huang, G. Yu, *Nano Lett.* 9 (2009) 1752-1758.
- [36] F.C. Zheng, Y. Yang, Q.W. Chen, *Nat. Commun.* 5 (2014) 5261-5270.
- [37] Y.R. Guo, Q. Liu, Z.H. Li, Z.G. Zhang, X.M. Fang, *Appl. Catal. B* 221 (2018) 362-370.

- [38] F.B. Su, J.H. Zeng, X.Y. Bao, Y.S. Yu, J.Y. Lee, X.S. Zhao, *Chem. Mater.* 17 (2005) 3960-3967.
- [39] Y.F. Song, J. Yang, K. Wang, S. Haller, Y.G. Wang, C.X. Wang, Y.Y. Xia, *Carbon* 96 (2016) 955-964.
- [40] J.J. Shi, M.S. Zhao, Y.Y. Wang, J. Fu, X.Y. Lu, Z.Y. Hou, *J. Mater. Chem. A* 4 (2016) 5842-5848.
- [41] H.X. Qu, X.J. Zhang, J.J. Zhan, W.Q. Sun, Z.C. Si, H.K. Chen, *ACS Sustainable Chem. Eng.* 6 (2018) 7380-7389.
- [42] M.H. Tang, J. Deng, M.M. Li, X.F. Li, H.R. Li, Z.R. Chen, Y. Wang, *Green Chem.* 18 (2016) 6082-6090.
- [43] X.J. Cui, A.E. Surkus, K. Junge, C. Topf, J. Radnik, C. Kreyenschulte, M. Beller, *Nat. commun.* 7 (2016) 11326-11333.
- [44] Q.L. Yao, Z.H. Lu, K.K. Yang, X.S. Chen, M.H. Zhu, *Sci. Rep.* 5 (2015) 15186-15196.
- [45] Z.Z. Wei, X.F. Li, J. Deng, J. Wang, H.R. Li, Y. Wang, *Mol. Catal.* 448 (2018) 100-107.
- [46] C. Moreno-Marrodan, F. Liguori, E. Mercadé, C. Godard, C. Claver, P. Barbaro, *Catal. Sci. Technol.* 5 (2015) 3762-3772.
- [47] Y.L. Cao, M.H. Tang, M.M. Li, J. Deng, F. Xu, L. Xie, Y. Wang, *ACS Sustainable Chem. Eng.* 5 (2017) 9894-9902.
- [48] G. Chacón, J. Dupont, *ChemCatChem* 11 (2019) 333-341.
- [49] M.L. Frauwallner, F. López-Linares, J. Lara-Romero, C.E. Scott, V. Ali, E. Hernández, *Appl. Catal. A* 394 (2011) 62-70.
- [50] M. Lijewski, J.M. Hogg, M. Swadźba-Kwaśny, P. Wasserscheid, M. Haumann, *RSC Adv.* 7 (2017) 27558-27563.
- [51] L.Z. Zuo, Y. Guo, X. Li, H.Y. Fu, X.L. Qu, S.R. Zheng, C. Gu, D.Q. Zhu, P.J. Alvarez, *Environ. Sci. Technol.* 50 (2015) 899-905.
- [52] J. Zakzeski, P.C.A. Bruijninx, A.L. Jongerius, B.M. Weckhuysen, *Chem. Rev.* 110 (2010) 3552-3599.
- [53] S. Srivastava, N. Solanki, P. Mohanty, K.A. Shah, J.K. Parikh, A.K. Dalai, *Catal.*

- Lett. 145 (2015) 816-823.
- [54] D.M. Zhu, H.B. Jiang, L. Zhang, X.L. Zheng, H.Y. Fu, M.L. Yuan, H. Chen, R.X. Li, *ChemCatChem* 6 (2014) 2954-2960.
- [55] Z.S. Ma, H.Y. Zhang, Z.Z. Yang, G.P. Ji, B. Yu, X.W. Liu, Z.M. Liu, *Green Chem.* 18 (201) 1976-1982.
- [56] F.W. Zhang, C.L. Ma, S.A. Chen, J.F. Zhang, Z.H. Li, X.M. Zhang, *Mol. Catal.* 452 (2018) 145-153.
- [57] J.J. Huo, R.L. Johnson, P. Duan, H.N. Pham, D. Mendivelso-Perez, E.A. Smith, A.K. Datye, K. Schmidt-Rohrbc, B.H. Shanks, *Catal. Sci. Technol.* 8 (2018) 1151-1160.
- [58] J.J. Huo, P. Duan, H.N. Pham, Y.J. Chan. A.K. Datye, K. Schmidt-Rohr, B.H. Shanks, *Catal. Sci. Technol.* 8 (2018) 3548-3561.

Figure and Table captions

Table 1. Physical properties and average particle sizes of different Ru catalysts.

Table 2. Hydrogenation of toluene over different catalysts.

Table 3. Hydrogenation of olefins, arenes and other biomass-derived molecules over the Ru/CN-SBA-15 catalyst.

Table 4. Hydrogenation of N-heterocyclic compounds over the Ru/CN-SBA-15 catalyst.

Fig. 1. (a) XRD patterns (b) Raman spectra of the different Ru catalysts.

Fig. 2. XPS spectra of (a) C 1s of Ru/C-SBA-15, (b) C 1s and (c) N 1s of Ru/CN-SBA-15, (d) N 1s of CN-SBA-15.

Fig. 3. XPS spectra: Ru 3p of Ru/SBA-15, Ru/C-SBA-15 and Ru/CN-SBA-15.

Fig. 4. FESEM images of different samples. (a) SBA-15, (b) Ru/C, (c) Ru/CN, (d) Ru/SBA-15, (e) Ru/C-SBA-15 and (f) Ru/CN-SBA-15.

Fig. 5. HAADF-STEM images and the particle size distribution of (a) Ru/C, (b) Ru/CN, (c) Ru/SBA-15, (d) Ru/C-SBA-15, (e) Ru/CN-SBA-15 and energy dispersive X-ray spectrum (EDS) of (f) Ru/CN-SBA-15.

Fig. 6. Turnover frequency (TOF) values of hydrogenation of toluene per total number of metal atoms as a function of the particle size obtained from HAADF-STEM images at the temperature of 343K, 353K, 363K and 373K.

Fig. 7. (a)-(c) Conversion/time profiles of hydrogenation reactions catalyzed by Ru

catalysts at different temperatures. (d) Arrhenius plots for the hydrogenation reaction of toluene. The observed rate constants (k) were calculated with the initial rates from Fig. 7 (a)-(c) at different temperatures. Reaction conditions: 2.6 mmol toluene, 20.0 mg catalysts; 3.0 mL H₂O, 2.0 MPa H₂.

Fig. 8. FTIR spectra of (a) Ru/CN-SBA-15, (b) Ru/CN-SBA-15 catalyst adsorbed with quinolone, (c) quinoline.

Fig. 9. The recyclability of Ru catalysts for hydrogenation of BPE to alicyclic ether. Reaction conditions: Substrate/Ru = 6500 (molar ratio), 80.0 mg catalysts, 3.0 mL H₂O, 12 h, 2.0 MPa H₂, 100 °C. (a) Ru/SBA-15, (b) Ru/C-SBA-15 and (c) Ru/CN-SBA-15.

Fig. 10. FESEM (top) and HAADF-STEM images (bottom) of the used Ru catalysts. (a) and (d) Ru/SBA-15, (b) and (e) Ru/C-SBA-15, (c) and (f) Ru/CN-SBA-15.

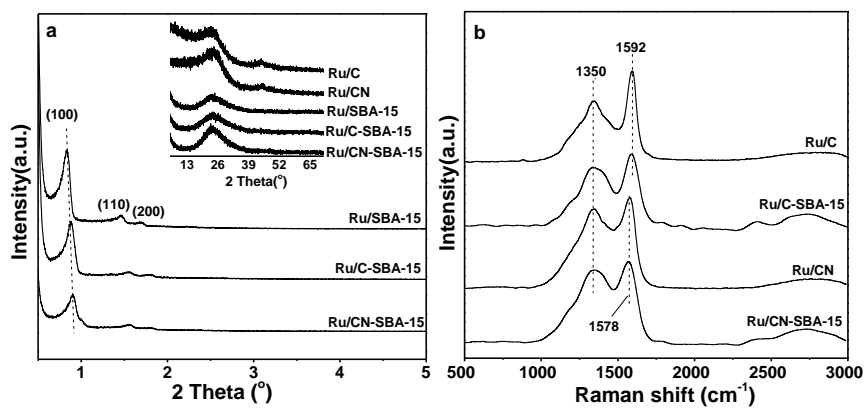


Fig. 1. (a) XRD patterns (b) Raman spectra of the different Ru catalysts.

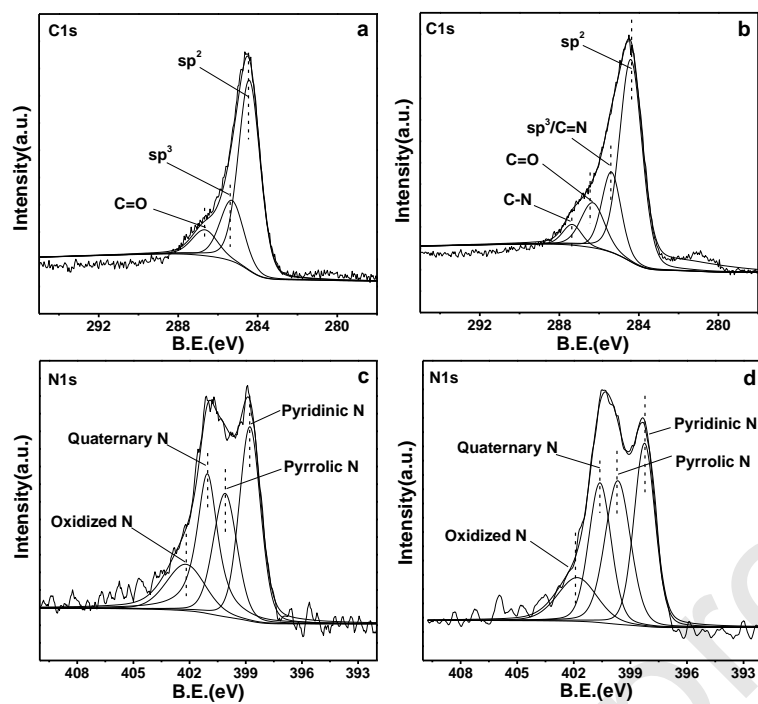


Fig. 2. XPS spectra of (a) C 1s of Ru/C-SBA-15, (b) C 1s and (c) N 1s of Ru/CN-SBA-15, (d) N 1s of CN-SBA-15.

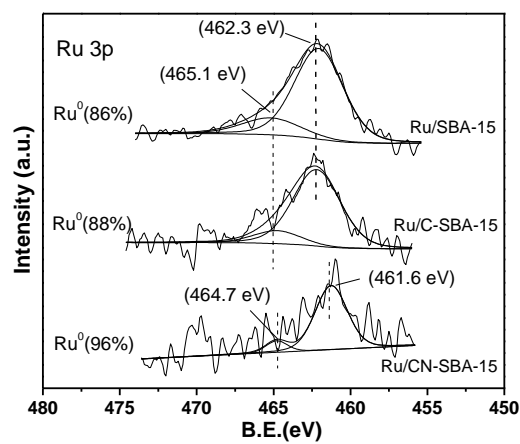


Fig. 3. XPS spectra: Ru 3p of Ru/SBA-15, Ru/C-SBA-15 and Ru/CN-SBA-15.

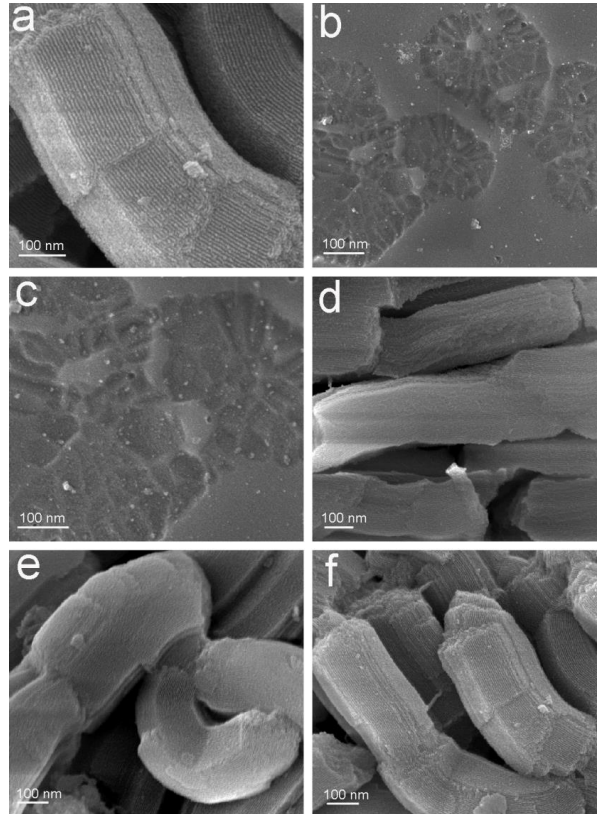


Fig. 4. FESEM images of different samples. (a) SBA-15, (b) Ru/C, (c) Ru/CN, (d) Ru/SBA-15, (e) Ru/C-SBA-15 and (f) Ru/CN-SBA-15.

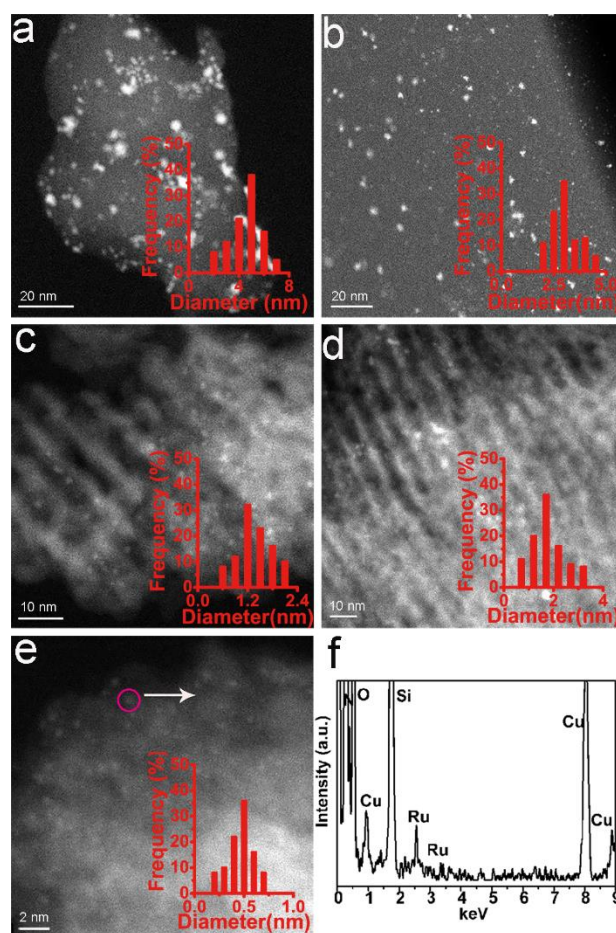


Fig. 5. HAADF-STEM images and the particle size distribution of (a) Ru/C, (b) Ru/CN, (c) Ru/SBA-15, (d) Ru/C-SBA-15, (e) Ru/CN-SBA-15 and energy dispersive X-ray spectrum (EDS) of (f) Ru/CN-SBA-15.

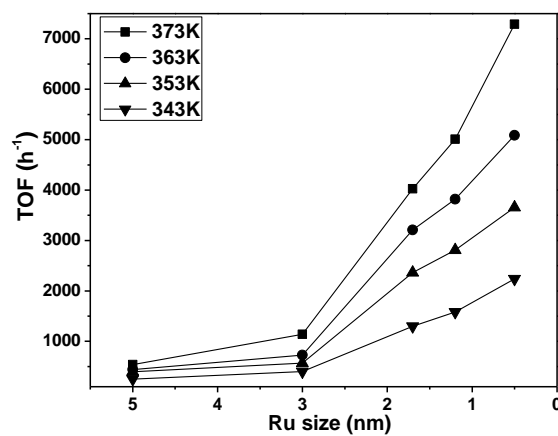


Fig. 6. Turnover frequency (TOF) values of hydrogenation of toluene per total number of metal atoms as a function of the particle size obtained from HAADF-STEM images at the temperature of 343K, 353K, 363K and 373K.

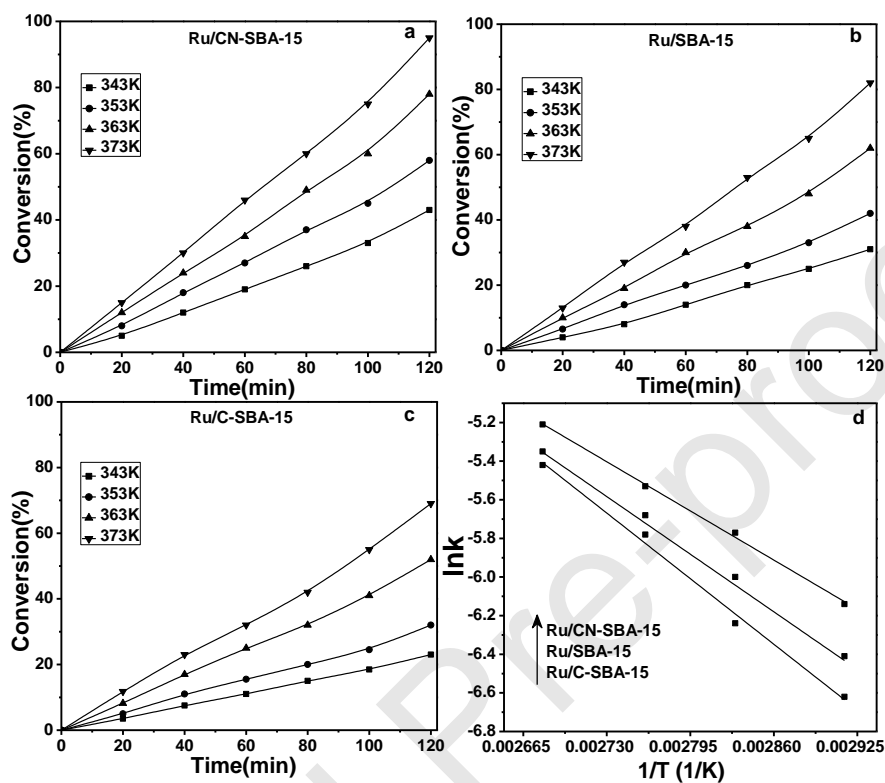


Fig. 7. (a)-(c) Conversion/time profiles of hydrogenation reactions catalyzed by Ru catalysts at different temperatures. (d) Arrhenius plots for the hydrogenation reaction of toluene. The observed rate constants (k) were calculated with the initial rates from Fig. 7 (a)-(c) at different temperatures. Reaction conditions: 2.6 mmol toluene, 20.0 mg catalysts; 3.0 mL H₂O, 2.0 MPa H₂.

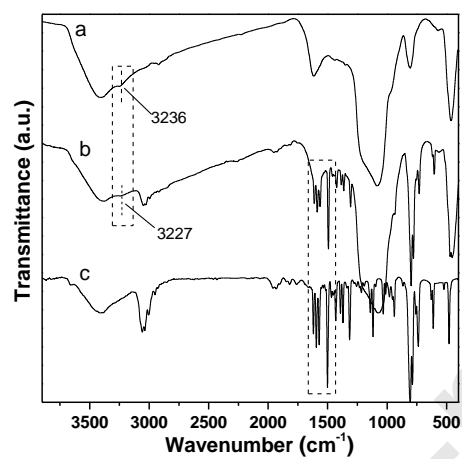


Fig. 8. FTIR spectra of (a) Ru/CN-SBA-15, (b) Ru/CN-SBA-15 catalyst adsorbed with quinolone, (c) quinoline.

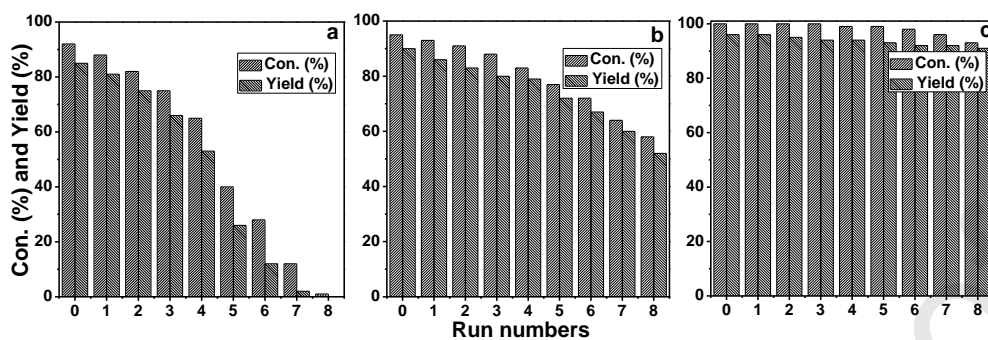


Fig. 9. The recyclability of Ru catalysts for hydrogenation of BPE to alicyclic ether. Reaction conditions: Substrate/Ru = 6500 (molar ratio), 80.0 mg catalysts, 3.0 mL H₂O, 12 h, 2.0 MPa H₂, 100 °C. (a) Ru/SBA-15, (b) Ru/C-SBA-15 and (c) Ru/CN-SBA-15.

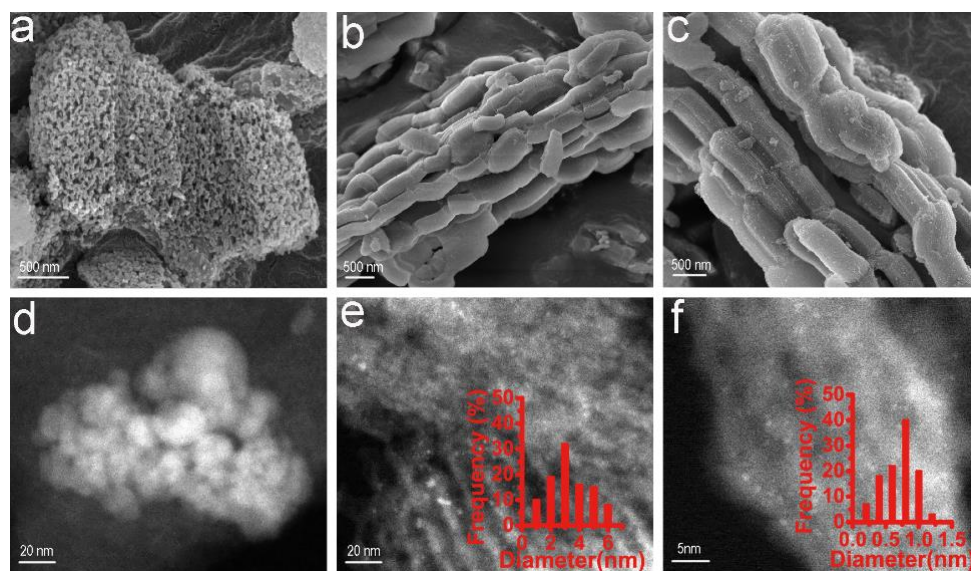


Fig. 10. FESEM (top) and HAADF-STEM images (bottom) of the used Ru catalysts. (a) and (d) Ru/SBA-15, (b) and (e) Ru/C-SBA-15, (c) and (f) Ru/CN-SBA-15.

Table 1. Physical properties and average particle sizes of different Ru catalysts.

Entries	Catalysts	$S_{\text{BET}}^{\text{a}}$ ($\text{m}^2 \text{g}^{-1}$)	$V_{\text{total}}^{\text{b}}$ ($\text{cm}^3 \text{g}^{-1}$)	Pore size ^c (nm)	Ru size ^d (nm)
1	Ru/C	<10	-	-	5.0
2	Ru/CN	<15	-	-	3.0
3	Ru/SBA-15	757	1.139	8.2	1.2
4	Ru/C-SBA-15	511	0.682	7.5	1.7
5	Ru/CN-SBA-15-1.32	508	0.623	7.4	1.1
6	Ru/CN-SBA-15-2.68	500	0.589	7.2	0.9
7	Ru/CN-SBA-15	498	0.556	7.0	0.5
8	Ru/CN-SBA-15-5.21	381	0.405	5.2	1.4

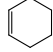
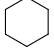
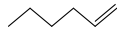
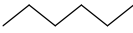
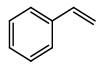
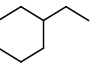
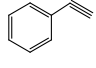
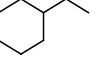
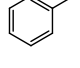
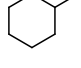
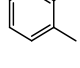
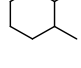
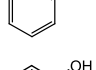
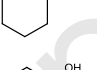
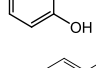
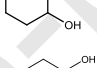
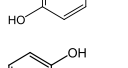
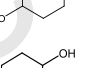
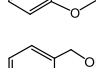
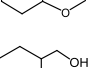
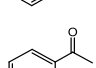
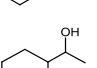
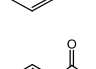
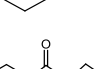
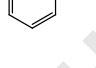
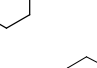
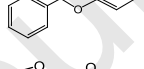
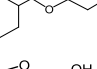
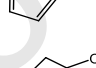
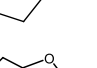

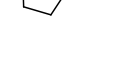
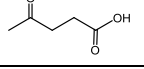
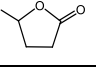
^aSurface area were calculated from the nitrogen adsorption isotherm using the BET method. ^bTotal pore volume was calculated from nitrogen sorption isotherms at $P/P_0 = 0.99$. ^cPore size was calculated by the BJH method. ^dThe mean size of Ru particles was calculated from HAADF-STEM images.

Table 2. Hydrogenation of toluene over different catalysts.

Entries	Catalysts	Water content (mL)	Times (h)	Yield (%)	TOF (h ⁻¹)
1	None	3	5	-	-
2	C-SBA-15	3	5	-	-
3	CN-SBA-15	3	5	-	-
4	Ru/C	3	5	30.0	538
5	Ru/CN	3	5	42.0	1136
6	Ru/SBA-15	3	3.5	>99	5072
7	Ru/C-SBA-15	3	4.5	>99	4026
8	Ru/CN-SBA-15	3	2.5	>99	7289
		5	2.5	95.5	7283
		7	2.5	95.0	7279
		9	2.5	94.5	7273
9 ^a	Ru/AC	3	5	>99	294

Conditions: 2.6 mmol toluene, 20.0 mg catalysts, 100 °C and 2.0 MPa H₂. The methylcyclohexane was detected as a sole product (entries 4-12). ^a5.0 mg Ru/AC (5 wt.%) was employed.

Table 3. Hydrogenation of olefins, arenes and other biomass-derived molecules over the Ru/CN-SBA-15 catalyst.^a

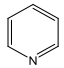
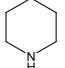
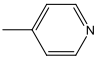
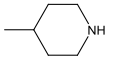
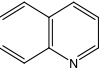
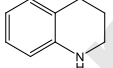
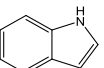
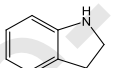
Entries	Substrates	T (°C)	P (MPa)	Time (h)	Products	Yield (%)	TOF (h ⁻¹)
1		60	1	2		>99	10288
2		50	1	1.5		>99	12026
3		60	2	2		>99	8273
4		60	3	4		>99	5511
5		100	2	3		>99	7289
6		100	2	5		>99	5298
7		80	2	4		>99	4623
8		80	2	6		>99	4148
9		80	2	6		>99	4159
10		80	2	6.5		>99	3808
11		100	3	3		>99	3705
12		100	3	4		95	3579
13		100	2	7		97	2298
14 ^b		100	2	9		96	1883
15		80	3	3		>99	2812
16		80	3	5		>99	2415
17		90	3	3		>99	4092

^aConditions: Substrates/Ru=13000(molar ratio), 3.0 mL H₂O, 20.0 mg Ru/CN-SBA-15.

The conversion was normally more than 99%. ^b40.0 mg Ru/CN-SBA-15 was used

(Substrates/Ru=6500).

Table 4. Hydrogenation of N-heterocyclic compounds over the Ru/CN-SBA-15 catalyst.

Entries	Substrates	T (°C)	P (MPa)	Time (h)	Products	Yield (%)	TOF (h ⁻¹)
1		90	2	6		>99	2689
2		100	2	7.5		>99	2106
3		100	3	12		>99	1509
4		100	3	10		>99	1793

Conditions: Substrates/Ru=5000(molar ratio), 3.0 mL H₂O, 40.0 mg Ru/CN-SBA-15.